Cost-effective IoT hyperspectral prototype for distributed agri-food product monitoring

Sara Vignati, Alessio Tugnolo, Marco Torrente, Alessia Pampuri, Riccardo Guidetti, Roberto Beghi, Valentina Giovenzana

Department of Agricultural and Environmental Sciences (DiSAA), University of Milan, Italy

Abstract

Hyperspectral imaging (HSI) is a non-destructive technique that is employed to assess quality parameters and integrate monitoring across the supply chain in the context of Industry 4.0. Although promising, HSI faces challenges such as high cost and equipment requirements. However, advances in technology and 3D printing are enabling low-cost solutions that still need to be validated in the field. This work presents the development of a low-cost hyperspectral prototype, built using 3D elements and commercially available electronic components, and operating in the spectral range from 400 nm to 1000 nm. Furthermore, two types of gratings have been compared. In the first part of the study, the calibration process using RGB LEDs and a halogen lamp is described in detail. The second part of the study presents the results of a few applications on a food matrix under controlled light conditions, which were conducted to evaluate the performance of the prototype. The extracted spectra were normalised and subsequently pre-processed with either standard normal variate (SNV) transform or the Savitzky-Golay (SG) derivative. Finally, the data were explored with principal component analysis (PCA), which confirmed the ability of the prototype to distinguish samples of different colours (first trial), assess the decay of different apple samples (second trial) and differentiate between healthy and damaged tissues (third trial). The experimental results were consistent with the anticipated outcomes, and both types of grating demonstrated favourable performance.

Correspondence: Alessio Tugnolo, Department of Agricultural and Environmental Sciences (DiSAA), University of Milan, via Celoria 2, 20133 Milan, Italy. E-mail: alessio.tugnolo@unimi.it

Key words: hyperspectral imaging; IoT sensors; portable; low-cost; process monitoring.

Contributions: all authors made a substantive intellectual contribution, read and approved the final version of the manuscript and agreed to be accountable for all aspects of the work.
Conflict of interest: the authors declare no competing interests, and all authors confirm accuracy.

Received: 13 December 2024.
Accepted: 29 April 2025.

©Copyright: the Author(s), 2025
Licensee PAGEPress, Italy
Journal of Agricultural Engineering 2025; LVI:1664
doi:10.4081/jae.2025.1664

This work is licensed under a Creative Commons Attribution-NonCommercial 4.0 International License (CC BY-NC 4.0).

Publisher's note: all claims expressed in this article are solely those of the authors and do not necessarily represent those of their affiliated organizations, or those of the publisher, the editors and the reviewers. Any product that may be evaluated in this article or claim that may be made by its manufacturer is not guaranteed or endorsed by the publisher.

Introduction

The food quality refers to sensory aspects, shelf-life and freshness, nutrient contents, and also microbiological and technological features (Hassoun *et al*., 2023).

Nowadays, quality process control in agri-food production has significantly evolved, particularly with the integration of laboratory-grade analytical instrumentation directly into processing lines (at-line, on-line, and in-line). These technologies offer the potential for real-time monitoring and rapid decision-making, improving product consistency and reducing waste. However, despite these advantages, the practical implementation of such systems remains challenging. The complexity of the equipment, the need for specific environmental conditions (e.g., vibration-free, temperature-stable settings), and the requirement for trained personnel often limit their usability in standard industrial environments. Factors such as high initial investment costs, maintenance demands, and integration difficulties with existing production workflows further hinder widespread adoption. As a result, many production facilities, particularly small to medium-sized enterprises (SMEs), still rely on more traditional, off-line quality control methods, which are less efficient and delay corrective actions.

In the last two decades, hyperspectral imaging (HSI) technology has been emerging as a very potential non-destructive optical tool for food quality and safety assessment in post-harvest, adding a new component to reduce the gap between laboratory analyses and the production process as a process analytical technology (PAT) (Vignati *et al*., 2023). Moreover, this is playing a key role in the Fourth Industrial Revolution ("Industry 4.0"), which is enhancing the use of interconnected sensor networks (Internet of Things - IoT) and digital innovations and techniques (e.g., machine learning, big data, and cloud) in monitoring systems (Hassoun *et al*., 2022, 2023).

These sensors network results in a multivariate statistical process control (MSPC) which provides, for each critical point of the production chain, several highly correlated variables (both optical and not), that can be handled by multivariate projection methods (such as principal component analysis – PCA), allowing a reduction in data dimensionality by utilizing the correlated structure (Kourti, 2006). Taking for example the fruit and vegetables or the fresh-cut supply chains, an optimised system of sensors interconnected may be applied to monitor the entire production process,

from the cultivation phase, in both field and greenhouse, to the different post-harvest processing steps. This will lead to some advantages such as: i) the creation of remote storage of optical data, ensuring a continuous updating and refinement of the models to constantly improve the monitoring at critical points of the supply chain and the decision-making process, both in farming and in industry (Pampuri *et al*. (2021b), Hassoun *et al*., 2022); ii) increase of the product shelf-life and, consequently, decreasing food losses and wastes (Casson *et al*., 2022); iii) assurance of a complete control along the entire supply chain (Vignati *et al*., 2023).

However, the hyperspectral imaging systems available at the moment on the market are laboratory instruments and portable devices and costs remain a limit for real applications of these tools (Pampuri *et al*., 2021a). Moreover, although the HSI technique allows to collection of a large amount of data, it may not be possible to control all critical points of the supply chain with a single instrument, but more devices are needed. This leads to prohibitive costs for most companies.

Cost reduction is a current challenge for industry and hence for researchers (Özdoğan *et al*., 2021; Giovenzana *et al*., 2015) and the first solution proposed was to build low-cost multispectral devices based on wavelength previously selected. This approach has some disadvantages, such as the limitation of the re-customization of the instrument and its applications on different kinds of products and of the ability to improve the predictive models.

Moreover, due to the fast and high technological advancements that occurred in the last ten years, such as the mass production of silicon detectors for commercial cameras and smartphones and miniaturized optical components, research is heading towards the development and testing of stand-alone, compact, cost-effective, and remotely controlled HSI devices.

Of these devices, there are some examples in literature. Habel *et al*. (2012) proposed one of the first low-cost and compact hyperspectral camera. The device design is based on a consumer camera, and it is a snapshot system based on computed tomography principles, according to which a transmissive diffraction grating is used by computed tomography image spectrophotometers (CTISs) to split the incoming light into many spectrum projections onto a single image plane. Then, the spectra are obtained by resolving an under-determined linear system. The prototype operates in the Visible-Near InfraRed (VNIR) spectral range and allows obtaining images with a spatial resolution of 120x120 pixels and a spectral resolution of up to 5 nm.

Taking advantage of the introduction of 3D printing, the advancement of optical and electronic components, and the popularity of compact, high-resolution cameras like the Raspberry PI NoIR camera, Salazar-Vazquez and Mendez-Vazquez (2020) suggested a cost-effective (around $500) and lightweight (300 g) HSI device. The camera operates in the wavelength range of 400 to 1052 nm and produces images with 116x110 pixels of spatial resolution and up to 2 nm of spectral resolution. The authors also developed a user-friendly graphical user interface, but the device exhibits low performance in the 750-1000 nm spectral range, suggesting a reduced analytical capability in food quality inspection, probably due to the type of dual-axis holographic transmissive grating used.

Another example of a cost-effective tool is the one built by Stuart *et al*. (2020), which utilises miniaturised and low-cost imagers and commercially available components that were recently developed. This device works in the visible range of the electromagnetic spectrum (340-850 nm) with a spectral resolution of 15 nm. Experiments conducted in laboratory conditions demonstrated that this hyperspectral sensor has potential application in a variety of fields ranging from the detection of bruises on fruit to the characterization of rocks.

The same tests were performed with good performances using an affordable and portable HSI device with smartphone-based components (Stuart *et al*., 2021). In this study, a transmissive diffraction grating was used, but a handling system was required to analyse the entire sample and construct the hypercube. As in the previous work, the device covers the visible spectral range (400-700 nm) effectively, but the detectable optical range is shortened by IR filters found on common smartphone cameras. There are other examples reported in the literature, like the works by Sigernes *et al*. (2018), Riihiaho *et al*. (2021), and Davies *et al*. (2022). However, the performances of these devices still need to be meticulously assessed, both in controlled and operational conditions, in order to demonstrate their applicability in pre- and post-harvest contexts. The development of cost-effective hyperspectral systems that can cover a broader spectral range from visible (400 nm) to NIR (1000 nm) is still ongoing. Based on these considerations, this work aims to build an HSI camera prototype working in the VNIR spectral range, portable, low-cost, and user-friendly, starting from indications given in the previous work by Salazar-Vazqueza and Mendez-Vazquez (2020). The aim of this paper is to develop a prototype of a cost-effective (500-1000 €) hyperspectral IoT device for monitoring the quality of agri-food products along the entire production chain, from the field to the industry considering also the distribution phase.

Materials and Methods

This section provides a detailed description of the proposed hyperspectral device, the calibration process and an acquisition test aimed at evaluating the performance of the prototype.

Hyperspectral camera prototype

The proposed device has been built combining in-house 3D printed parts (housings, case, *etc*.,) and commercially available electronic components. The 3D drawings were designed using the Autodesk Inventor package (software CAD 3D Inventor®, 2023) and subsequently printed using a UV resin-based LCD 3D-printer (Anycubic, Photon Mono X) with a resolution of 50 microns. The Anycubic Photon Workshop software has been used for the slicing step before printing. Figure 1 shows the different components of the hyperspectral device. In detail, the 3D elements are the following. The main case (Figure 1 A.1), lid (Figure 1 A.9) and spacers (Figure 1A 4,7,8) were used with the purpose to block the optical and electronics components and keep a constant distance (100 mm) between the frontal lens and the diffraction grating. To regulate the amount of light crossing through the optical system, a square aperture (Figure 1 A.3) has been inserted in the middle of the system. Three supports were used to hold the frontal lens (Figure 1 A.2), the Vis/NIR camera (Figure 1 A.6), and the diffraction grating (Figure 1A 5a,5b). To instantaneously split the broadband light into different wavelengths without moving parts, two types of single-axis diffraction gratings, differentiated by their material composition (and consequently the cost), were utilized to separate polychromatic light into its component wavelengths in transmission mode. The light dispersion is calculated using the following equation (1):

$$nl = d(\sin a + \sin b) \quad \text{(Eq. 1)}$$

where: n is an integer value describing the diffraction order, l is the diffracted monochromatic light's wavelength, d is the spacing between the grating grooves, a is the angle of the incident light (a is 0° in case of transmission gratings) and b is the diffracted angle of the monochromatic light leaving the grating (Palmer and Loewen, 2005) (Figure 2).

The first grating was a low-cost holographic polyester model (Figure 1B.10; Model 01307, Edmund Optics Inc., Barrington, NJ, USA), while the second one was a glass-based (B270® ultra-white glass by SCHOTT) grating (Figure 1B.11; Model 49580, Edmund Optics, Inc.). The dimensions of the holographic grating were 50.80 mm x 50.80 mm x 0.003 mm (L x W x T), and the glass grating measured 25.00 mm x 25.00 mm x 3.00 mm (L x W x T). Both types of gratings operate within the VNIR range (400-1000 nm), with a percentage of absolute transmission efficiency that vary according to the wavelength and the number of grooves (500 and 600 grooves/mm for the holographic and the glass grating, respectively) that compose the grating. Additionally, the setup included a fixed focal length frontal lens from the C Series (Model 59872, Edmund Optics Inc; Figure 1 B.14) and a Macro +10 lens with a

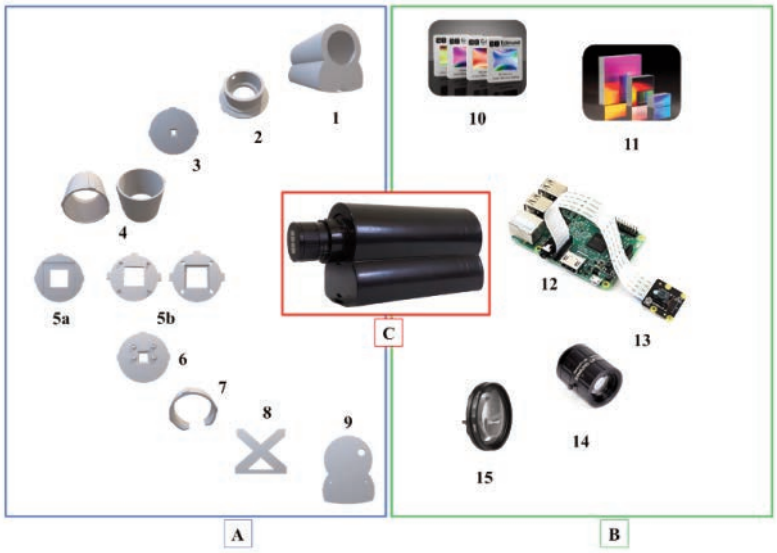


Figure 1. The hyperspectral prototype. **A**) 3D-printed components: 1. main case; 2. frontal lens hold; 3. square aperture; 4. spacers; 5a. holder of the holographic polyester grating; 5b. holder of the glass-based grating; 6. RaspiCam support; 7. 8. spacers: 9. lid. **B**) Commercially available: 10. holographic polyester grating; 11. glass-based grating; 12. Raspberry Pi 3B+; 13. Raspicam NoIR v2.1; 14. front lens; 15. macro +10 lens. **C**) Assembled prototype.

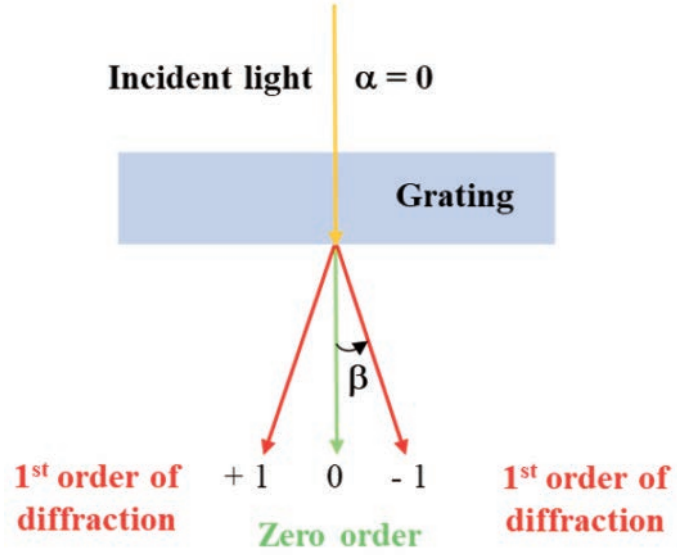


Figure 2. Physical working principle of a transmission grating to instantaneously split the broadband light.

52 mm diameter (Figure 1 B.15) to focus the sample onto the VNIR camera. The camera, a Raspicam NoIR v2.1 with a resolution of 1280x720 pixels and 8 MP (Figure 1 B.13), was controlled by a Raspberry Pi 3B+ (Figure 1 B.12).

The assembled VNIR hyperspectral prototype weighs approximately 500 grams and it has dimensions of 0.185 m x 0.065 m x 0.08 m (L x W x H). The device's small size and light weight make it particularly suitable for use in situations where portability is essential, such as environmental surveying, precision agriculture, and food quality monitoring. This allows operators to easily transport the device and perform quick and accurate measurements directly right on the spot without the need for bulky equipment. Furthermore, careful integration of optical and electronic components is required to ensure high performance without compromising portability.

Setup of the prototype

The hyperspectral prototype has been calibrated in a darkroom to prevent any interference from ambient light, ensuring that the device captures images solely from light sources emitting at specific wavelengths. These wavelengths include 632 nm (R), 522 nm (G), and 462 nm (B), using addressable LEDs to define the pixel positions in the image of such wavelengths. Additionally, a halogen lamp has been used to establish the upper and lower limits of the detectable spectral band, approximately 400-1000 nm. The camera holder, prototype, and light sources (LEDs and halogen) were positioned in darkroom. As shown in Figure 3, the prototype is placed at 0.40 m from the addressable LEDs (RGB-WS2812B), controlled by a Raspberry Pi Pico, and the halogen lamp. To ensure minimal light source reaching the detector, the light sources were covered with a layer of aluminium foil punctured using a thin needle (hole with a diameter ≤1 mm).

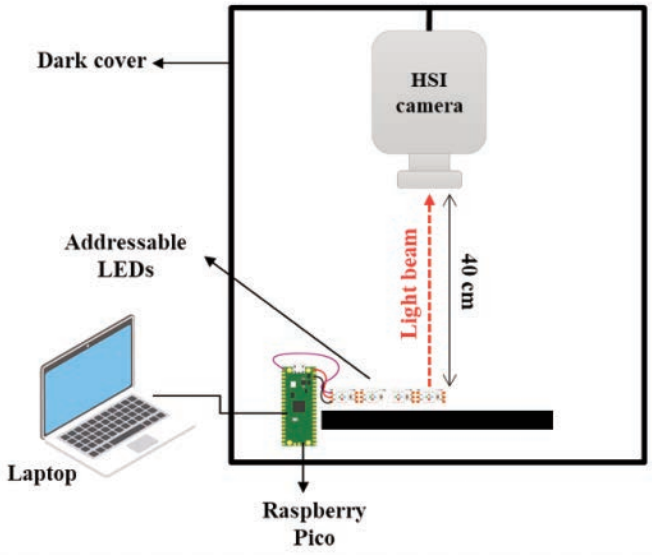


Figure 3. Schematic representation of the calibration acquisition set-up.

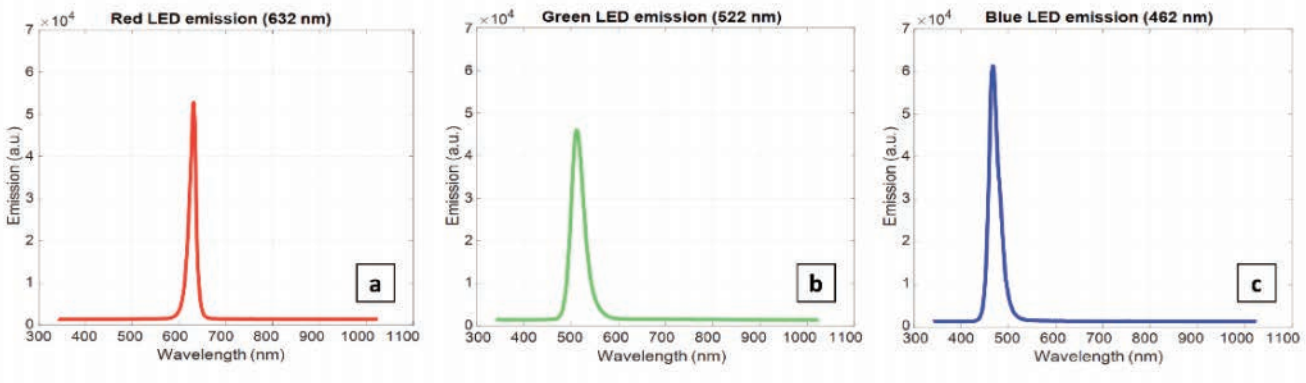


Figure 4. Emission peaks of the RGB channels detected with JAZ Spectrometer.

The prototype was connected to a portable computer through a smartphone hotspot and controlled in Matlab® environment, version 2023b (The MathWorks, Inc., Natick, MA, USA) using both built-in and in-house functions. Five calibration images were collected to identify the image Region of Interest (ROI), and to determine the extensions and the resolution of the diffracted spectrum. The halogen lamp served dual purposes acquiring under two different environmental conditions. The first image was obtained by acquiring with the halogen lamp without darkroom and aluminium cover. Such a method allowed to highlight in the image the effective ROI where to extract the spectral information for each pixel. The second image was acquired inside the darkroom with the lamp covered with the punctured aluminium foil. In this manner it was possible to identify, in the image, the extensions of the diffracted spectrum (first order of diffraction) in the VNIR region. Finally, a third, fourth, and fifth image were captured inside the darkroom using the LED emission in the R, G, and B channels to identify each emission peak with a known wavelength within the visible range of the spectrum. A commercial spectrophotometer (JAZ Spectrometer, Ocean Insight, JAZ Spectrometer Handheld Spectrometer, 450 to 1100 nm) was used to characterize the emission peaks of the RGB channels (Figure 4). Lastly, the images were post-processed starting from the first image without darkroom, from which the central ROI and the respective centroid were identified. Subsequently, the centroids were also detected for the diffraction of the R, G, and B channels in the corresponding wavelength peaks (632 nm, 522 nm, and 462 nm). However, by overlaying the image containing the ROI and those with the centroids of the RGB channels, a shift of the ROI barycentre was observed. This was due to the acquisition in the absence of a darkroom of the first image. Thus, the centroids were repositioned for both the ROI and the RGB channels and the individual areas in the diffracted spectrum corresponding to each channel are identified. This procedure has been done for both types of gratings (Figure 1 A 5a,b) in order to evaluate their performances and choose the better one.

Test in lab-scale and statistical analyses

Once calibrated, the hyperspectral prototype has been tested in lab-scale. An acquisition stage was developed to standardize the image acquisition. The set-up comprised: i) an optical bench (to correctly position the prototype, light sources and sample at certain distances), ii) a camera and a sample supports, iii) two halogen lamps with a 45° angle to the sample plane, and iv) a black cover to avoid interferences from the environmental light (Figure 5). The

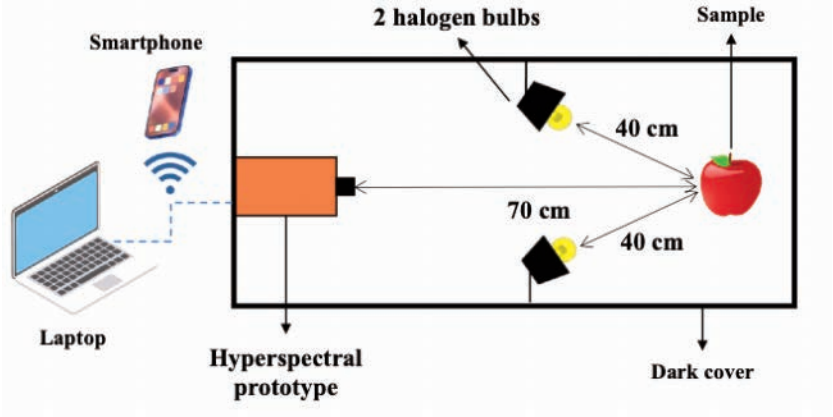


Figure 5. Schematic representation of the acquisition set-up used for the testing phase.

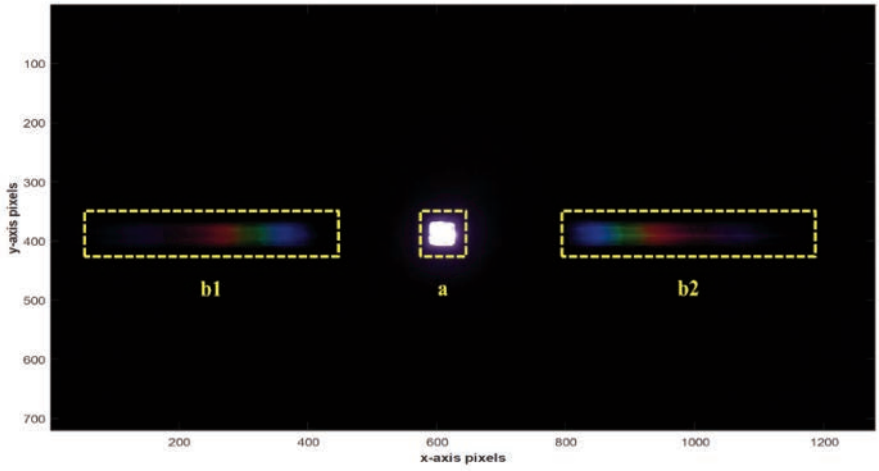


Figure 6. ROIs of the halogen light source image obtained with the polyester grating: zero order image (**a**); right (**b1**) and left (**b2**) first order of diffraction.

hyperspectral prototype was positioned 0.70 m from the object under analysis to capture its entirety within the frame. The light source was placed 0.40 m from the sample, with two different power settings, in order to avoid signal saturation: 4.0 V for the camera using the glass-based grating, and 5.3 V for the device with the plastic grating. The power values were obtained following the execution of acquisition tests on a white reference. Saturation of the acquired signal was evaluated and avoided for both gratings at the aforementioned power settings.

Three tests (with both grating types) were carried out using a food matrix to evaluate the prototype performance to detect spectral differences in such samples.

A first test was carried out acquiring images of three apples of different colours (*i.e.*, yellow, red, and green) to evaluate the capability of the system to maintain the performance of conventional RGB cameras. A second tests aimed to acquire images of 12 apples (three replicates each) with four different colours (*i.e.* yellow, red, green and yellow-red) at different time points (at the time of purchase, and after 15 and 30 days). A final tests, was performed to determine the ability of the prototype distinguishing between sound and damaged tissues. Images of 3 yellow healthy apples (three replica for each sample) were acquired. Subsequently, the fruits were damaged subjecting them to a simulated accidental post-harvest mechanical damage by dropping them to the ground from a height of 0.50 m. After 15 and 30 days images of the damaged apples were acquired, like in the experiment described above.

In each test, a white and dark reference images were taken, before acquiring three images for each sample. From each image, 42 diffracted spectra were extracted. Afterwards, every sample spectrum was normalized based on the white and dark references, using the following equation (2):

$$R = \frac{R_0 - D}{W - D} \cdot 100 \quad \text{(Eq. 2)}$$

where: R is the normalized spectrum (expressed in reflectance percentage), R_0 is the original spectrum, D is the dark reference spectrum, and W is the white reference spectrum. After normalization, the spectra obtained from each collected image were averaged before data pre-processing. This involved applying the standard normal variate (SNV) or Savitzky-Golay (SG) derivative to correct baseline vertical shifts, offsets, and global intensity effects typically caused by unwanted light scattering. Subsequent scaling was performed by mean-centering the data column-wise to minimize location differences between spectral variables. Finally, the spectra were explored using PCA. The data analyses were performed in Matlab® environment, version 2019b (The MathWorks, Inc.) using the PLSToolbox package (Eigenvector Research, Inc. Manson, Washington, USA) and in-house functions.

Results

Calibration images

During the calibration phase, five images were captured within a region of interest. Each captured images consisted of three distinct components: the central region defined as zero order (image of the scanned object), and the first orders (negative on the left and positive on the right) of the diffracted image. The first image has been acquired using a free source of light coming from a halogen light source (Figure 6). Such image acquisition aimed to define the ROI dimensions (1280 x 720 pixels) were the zero and first order of diffraction are contained. The central section shows the zero-order image (non-diffracted), representing the halogen light source in 42x42 pixels (Figure 6a). On either side, the first order of diffraction (Figure 6 b1,b2) displays the diffracted light from the source.

Therefore, the real image information has been linearly diffracted (both on the left and right respect to the central region) into the wavelengths that compose the VNIR optical range. No wavelength attribution to each pixel and the width of the VNIR range within the ROI diffraction portion can be extracted at this stage.

Once the ROI has been identified, three images were acquired using the addressable LEDs. The first-order diffraction regions helped pinpoint the exact pixel corresponding to each LED emission wavelength. Figures 7 and 8 show the LEDs images ROI (a1, b1, c1) and the pixels intensity (from 0 to 255), corresponding to the LED depicted in the zero order and its projection in the diffraction regions (a2, b2, c2), obtained with the plastic and the glass-based grating, respectively. In both cases, the linear diffraction provides specular peaks starting from the middle one related to the zero order. The intensity of the diffraction peaks differs according to the power of the LED for each wavelength emission. Such results are consistent with the intensity of the emission measurement performed with the commercial spectrometer shown in Figure 4. Indeed, a higher intensity was obtained for the blue channel then decreased for the red and green channels. Moreover, the high intensity of the blue channel is also noticeable in the left part of Figure 7 c2 and in the right part of Figure 8 c2, where the second order of diffraction is noticeable with a significantly lower intensity compared to the first order. The start of the second order of diffraction marks the end of the first one which was used as reference to define the image area needed for extracting spectral information. After identification of the middle peaks, the broad VNIR range in the first diffraction order has been identified using the halogen light bulb. As mentioned, the calibration images were elaborated to determine the area of the central ROI and the centroids of the latter and of each area of diffraction of the RGB channel. However, a little shift of the ROI centroid was noticed, and it was due to the acquisition of the image without darkroom. Thus, all the centroids were repositioned (Figure 9, in pink). Once the area of the diffracted light (called *blob* – Figures 7 and 8 a1,b1,c1) has been detected, and confirmed that the centroid is also the point where the emission peak is located, the corresponding peak values (i.e. 632 nm, 522 nm and 462 nm, for R, G, B channels, respectively) were assigned at each barycentre. Finally, the ROI of each diffracted colour has been computed based on the new centroids (Figure 9, in blue, green and red). Once the pixel position of the RGB peaks and the extent of the two diffraction areas were known, each x-pixel of the first orders of diffraction was converted to wavelength (nm) using a simple straight-line equation, and 42 spectra (corresponding to the square aperture dimensions in pixels) were extracted, as shown in Figure 10.

Acquisition tests

In this section are reported the results obtained from the different tests performed on the apple samples.

Apples colour

Spectra extraction

A first test was conducted on three apples with different

colours (i.e., yellow, red and green) with the goal to preliminary assess the system's capacity to detect spectral differences between the different samples. As shown in Figure 11, differences between the three apples were found, including variations in shape, intensity, and peaks at specific wavelengths. For both gratings the yellow apples had a higher reflectance compared to the red and green apples, with a peak around 620 nm. The red apples showed a peak around 650 nm for the glass-based grating and around 720 nm with the polyester grating. Finally, the green apples were characterised by a peak at 530 nm (in the green spectral region) as well as the peak in the red spectral region like the yellow ones and the characteristic chlorophyll absorbance peak around 670-680 nm. Moreover, we can notice a baseline drift in the spectra obtained from the glass-based grating and a slight multiplicative effect in both cases.

PCA results

In both cases, the PCA was performed on the data pre-processed with SNV and most of the variance was explained by the first two Principal Components (PCs): PC1 (> 70.00%) and PC2 (around 20.00 %). The loadings (Figures 12a and 13a) indicated specific wavelengths (i.e., 530 nm, 600 nm, 620 nm, and 680 nm) corresponding to the characteristic reflectance or absorbance peaks of each sample group and able to distinguish the different colours. This was confirmed in the scores plot (Figure 12b and 13b), where three distinct groups corresponding to each type of apples have been identified: green (G), red (R), and yellow (Y).

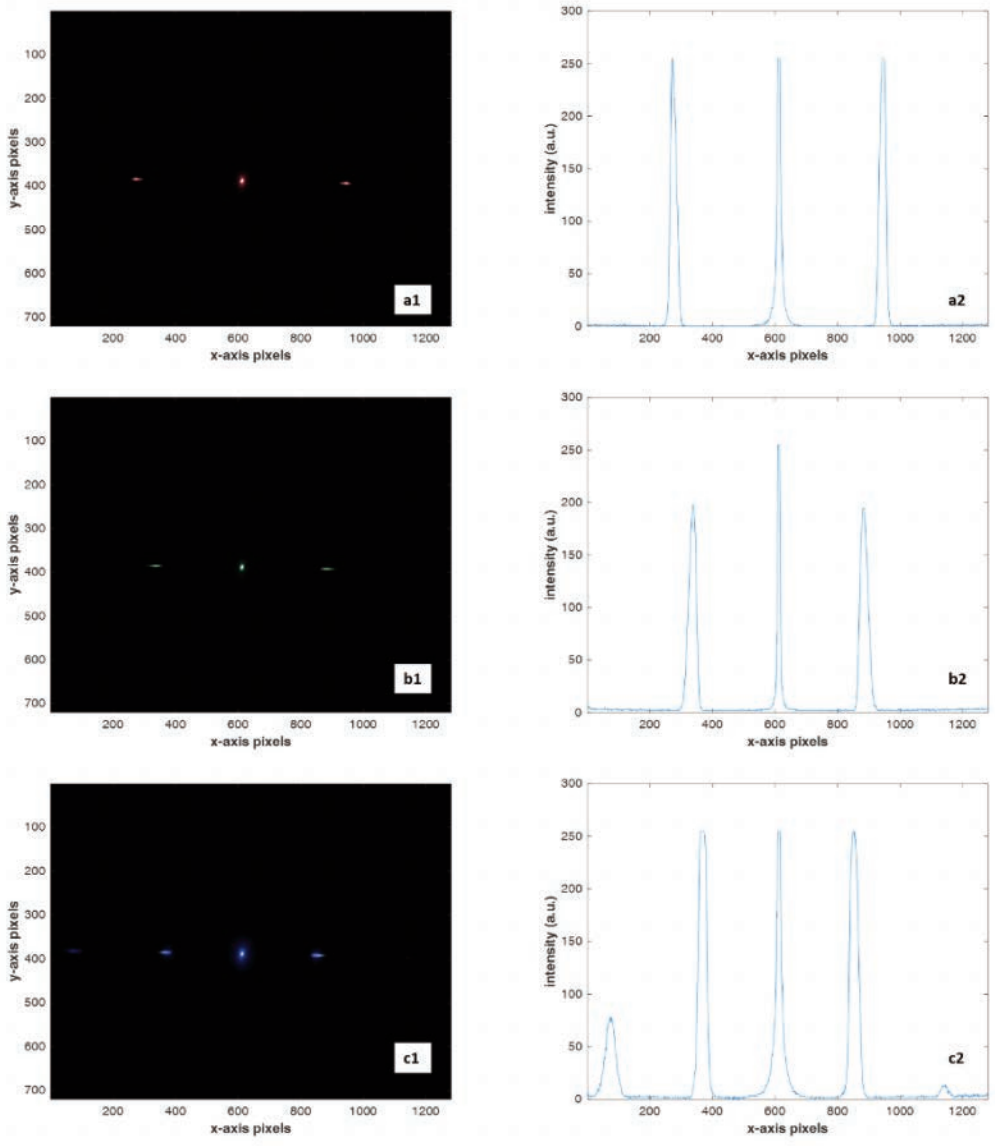


Figure 7. Comparison between the RGB images and their intensity graphs obtained with the polyester grating: **a1**) image of the red LED; **a2**) intensity graph of the R-image; **b1**) image of the green LED; **a2**) intensity graph of the G-image; **c1**) image of the blue LED; **c2)** intensity graph of the B-image.

Apple senescence

Spectra extraction

The second test was performed on apples at different time points to assess the prototype's ability to detect spectral differences in the samples during senescence. A general decrease in reflectance and some changes in spectra shape were observed, particularly with the glass-based grating as shown in Figure 14; while with the polyester grating a signal with more noise was obtained (Figure 15). Moreover, in the case of yellow and green apples, the signal occasionally reaches saturation. This phenomenon may be attributed to the enhanced light reflection capacity of these samples compared to other samples, as well as the potential inferior quality of the polyester grating.

PCA results

Firstly, the results on the PCA performed on the pre-processed spectra obtained from the glass-based grating are presented. A preliminary examination of the results revealed a distinct separation along PC1 of the three time points. Conversely, PC2 effectively differentiated fresh and healthy samples (i.e., t1) from those that have undergone senescence (i.e., t2 and t3) (Figure 16c). Some characteristic wavelengths could be identified combining both the pre-processed data plot (Figure 16a) and the loadings plot (Figure 16b), allowing the distinction between the various time groups. These wavelengths were: 500, 560, 580 and 630 nm. Furthermore, we could state that the colour of the apples was not related to the fruit's senescence, as no differentiation was observed across the various time points and sample types.

Regarding the polyester grating, the pre-processed data with SG first derivative and SNV (Figure 17a) and thus the loadings (Figure 17b) were characterised by high noise, especially in the NIR spectral region. Only PC1 allowed to highlight few peaks in

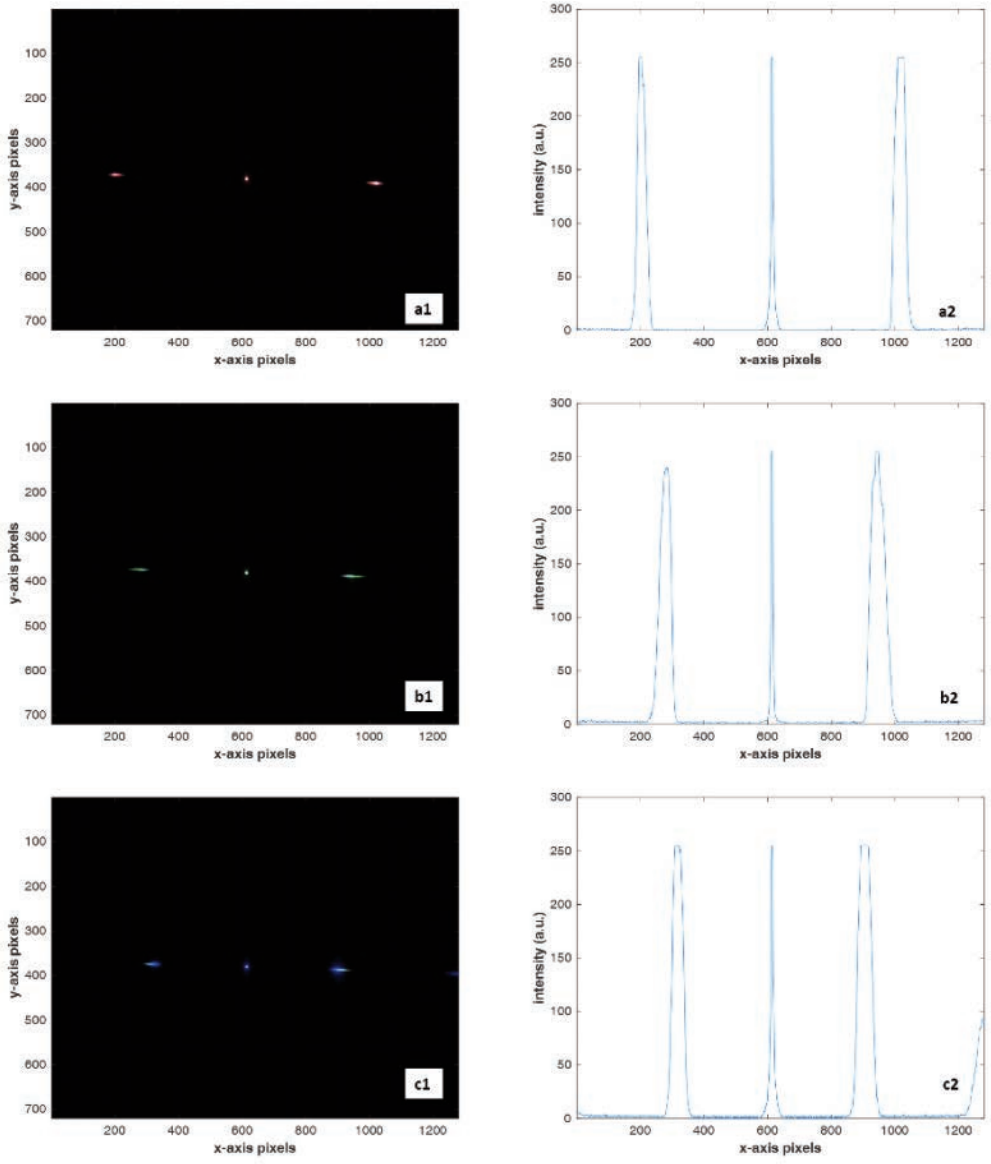


Figure 8. Comparison between the RGB images and their intensity graphs obtained with the glass-based grating: **a1**) image of the red LED; **a2**) intensity graph of the R-image; **b1**) image of the green LED; **a2**) intensity graph of the G-image; **c1**) image of the blue LED; **c2**) intensity graph of the B-image.

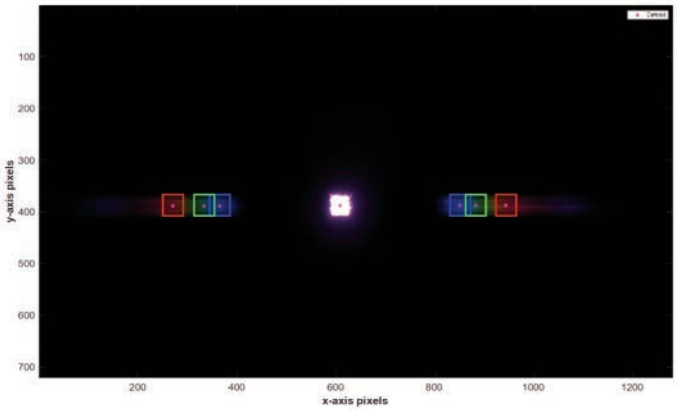


Figure 9. Image acquired without darkroom and the halogen lamp. It shows the Region of Interest (in the middle), the "adjusted" centroids (in pink) and the diffracted spectral area of each RGB channel (in blue for B-light, in green for G-light, in red for R-light).

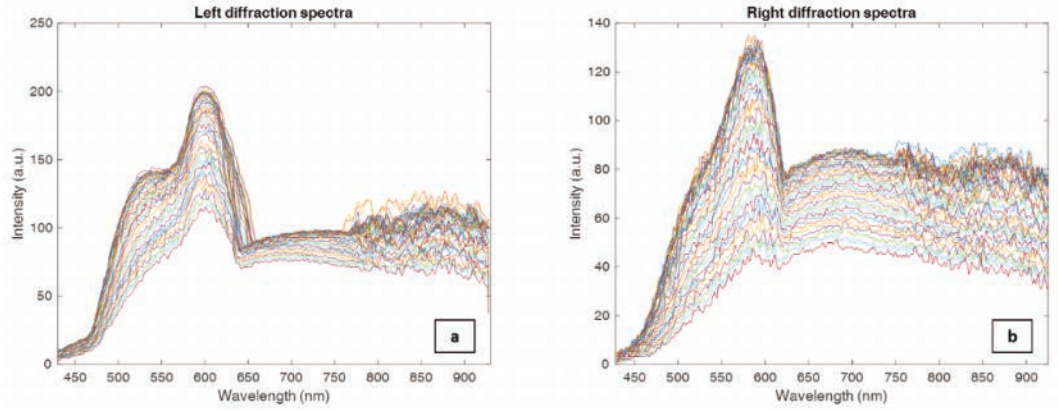


Figure 10. Diffraction spectra of the halogen lamp obtained using the glass-based grating: **a**) diffraction spectra of the left area of diffraction of the grating; **b**) diffraction spectra of the right area of diffraction of the grating.

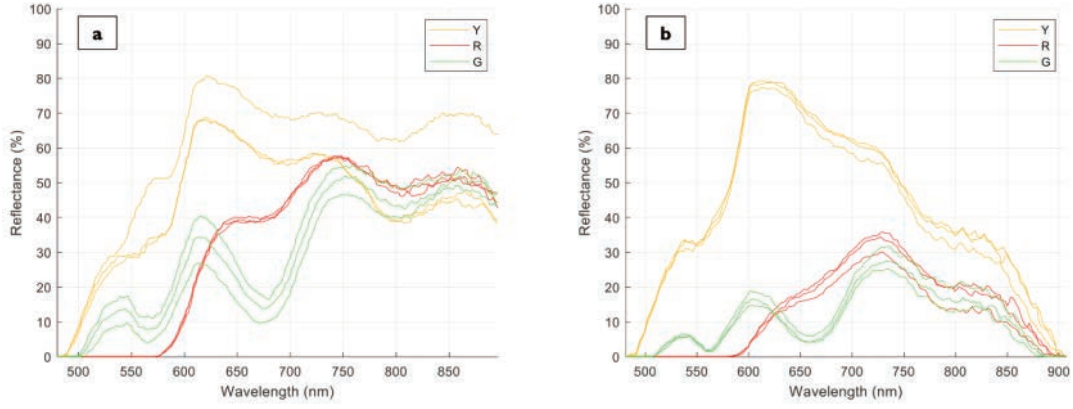


Figure 11. Normalized and averaged spectra of all the sample extracted from the left first order of diffraction obtained with (**a**) glass-based grating and (**b**) polyester grating.

the visible range between 450 and 600 nm (i.e., 460, 550, and 600 nm) able to distinguish between the three time points. This is confirmed in the scores plot (Figure 17c), where a differentiation between the time points can be observed only along PC1, despite t2 and t3 are inverted.

Healthy and damaged tissues in apples

Spectra extraction

From the last test performed, the spectra of the damaged tissues (i.e., D1 and D2) presented a general decrease in reflectance and some changes in the spectrum shape (e.g., a decrease in reflectance between 600-750 nm) compared to the healthy tissues (i.e., H), as shown in Figure 18. However, the spectra of the healthy tissues obtained with the polyester grating exceeded the normal levels of reflectance. This could be due to some light scattering or saturation of the signal during the acquisition step.

PCA results

Regarding the PCA performed on the dataset from the glass-based grating, a distinct separation between healthy and damaged tissue has been highlighted (Figure 19c), as well as the senescence progression of the damaged tissue over time (D1 to D2) (Figure 19d). Along PC1 the second stage of senescence (i.e., Damaged - t3) was separated from the healthy tissues (i.e., Healthy - t1) and the first stage of senescence (i.e., Damaged - t2), while along PC2 we obtained a good distinction between healthy and damaged tissues. According to the pre-processed data (Figure 19a) and the loadings plot (Figure 19b), the wavelengths highlighted on PC1 can be more related to the second stage of senescence. Indeed, the shape of the loadings is more akin to that observed in the Damaged - t3 group. Among the related wavelengths, we found 550 and 620 nm, which fall within the visible spectral range and are more closely related to fruit pigments. Additionally, there was a minor peak in the NIR spectral region, at 790 nm, which is more related to cell structure and tissue water content. On the contrary, the PC2 loadings exhibited a shape more similar to that of healthy tissue, with the highlighted wavelengths falling within the visible range and at 500, 530, 560, 590, 620 and 640 nm.

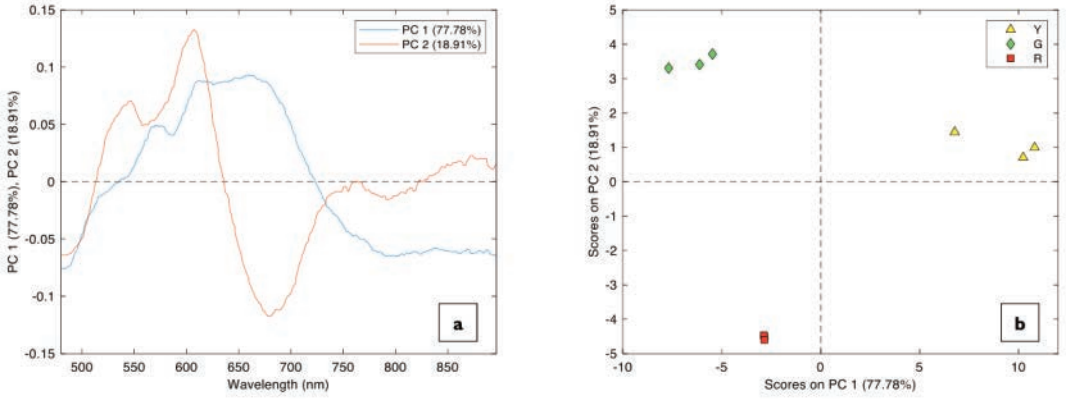


Figure 12. PCA performed on the spectra obtained with the glass-based grating: **a**) loadings plot; **b**) scores plot of the two first PCs.

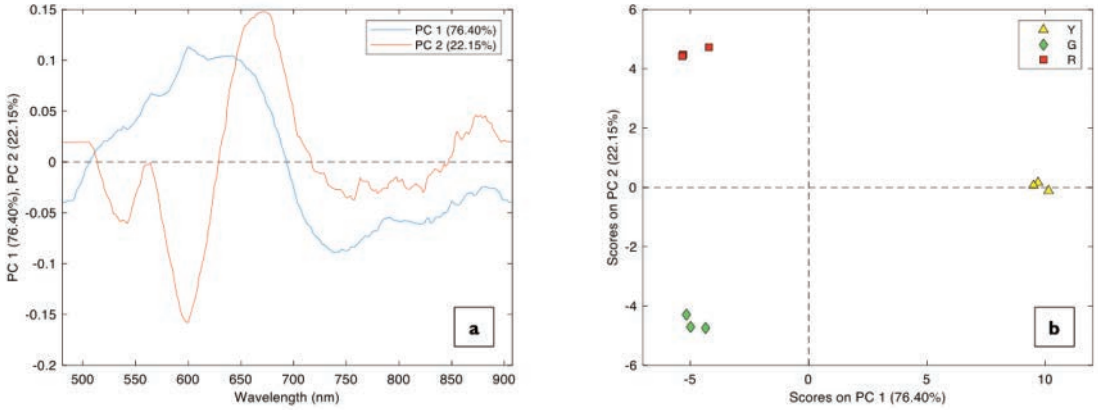


Figure 13. PCA performed on the spectra obtained with the polyester grating: **a**) loadings plot; **b**) scores plot of the two first PCs.

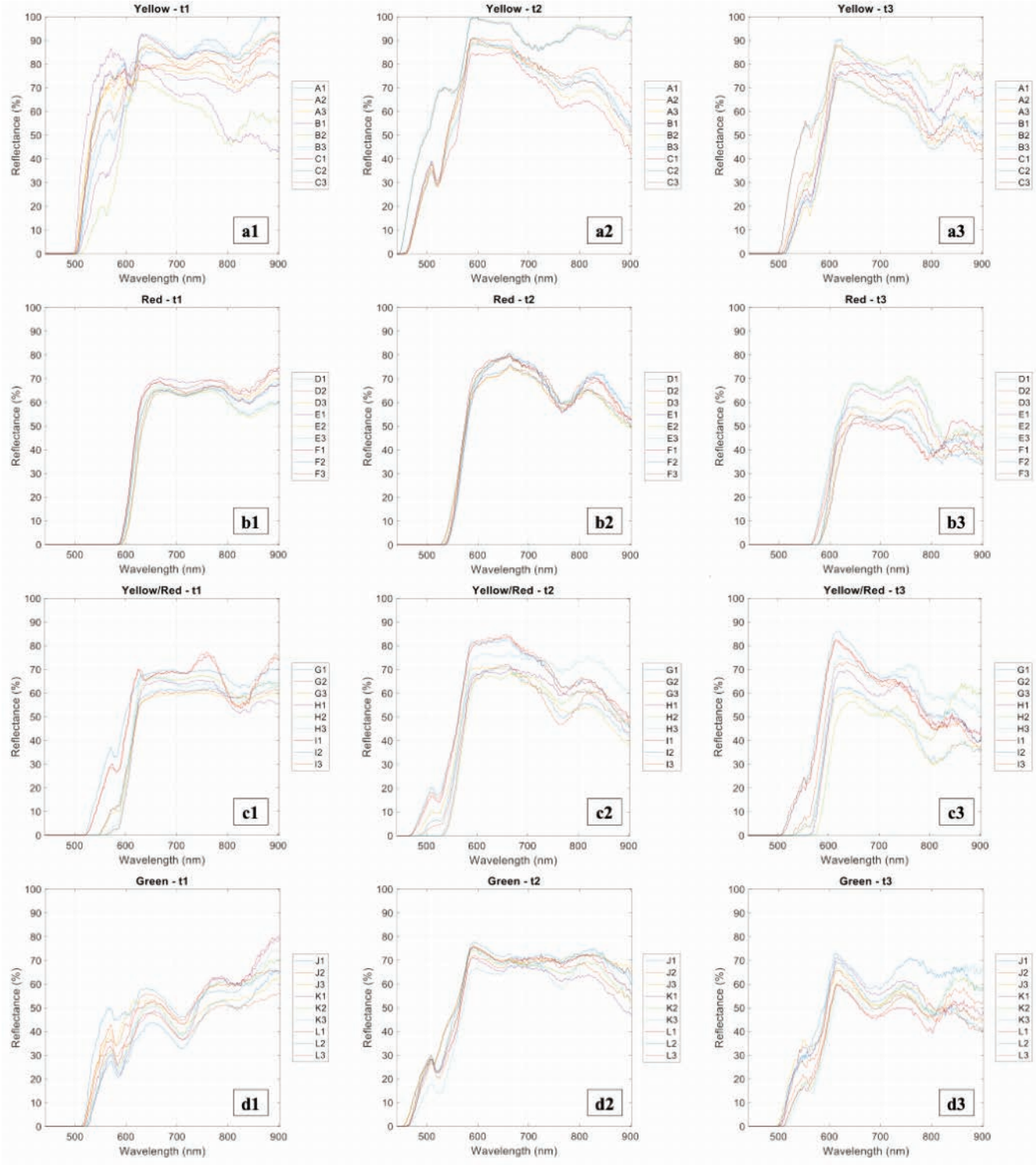


Figure 14. Normalized and averaged spectra extracted from the left first order of diffraction obtained with the glass-based grating at each time point (i.e., t1, t2, and t3): (**a**) yellow apples; (**b**) red apples; (**c**) yellow-red apples; (d) green apples.

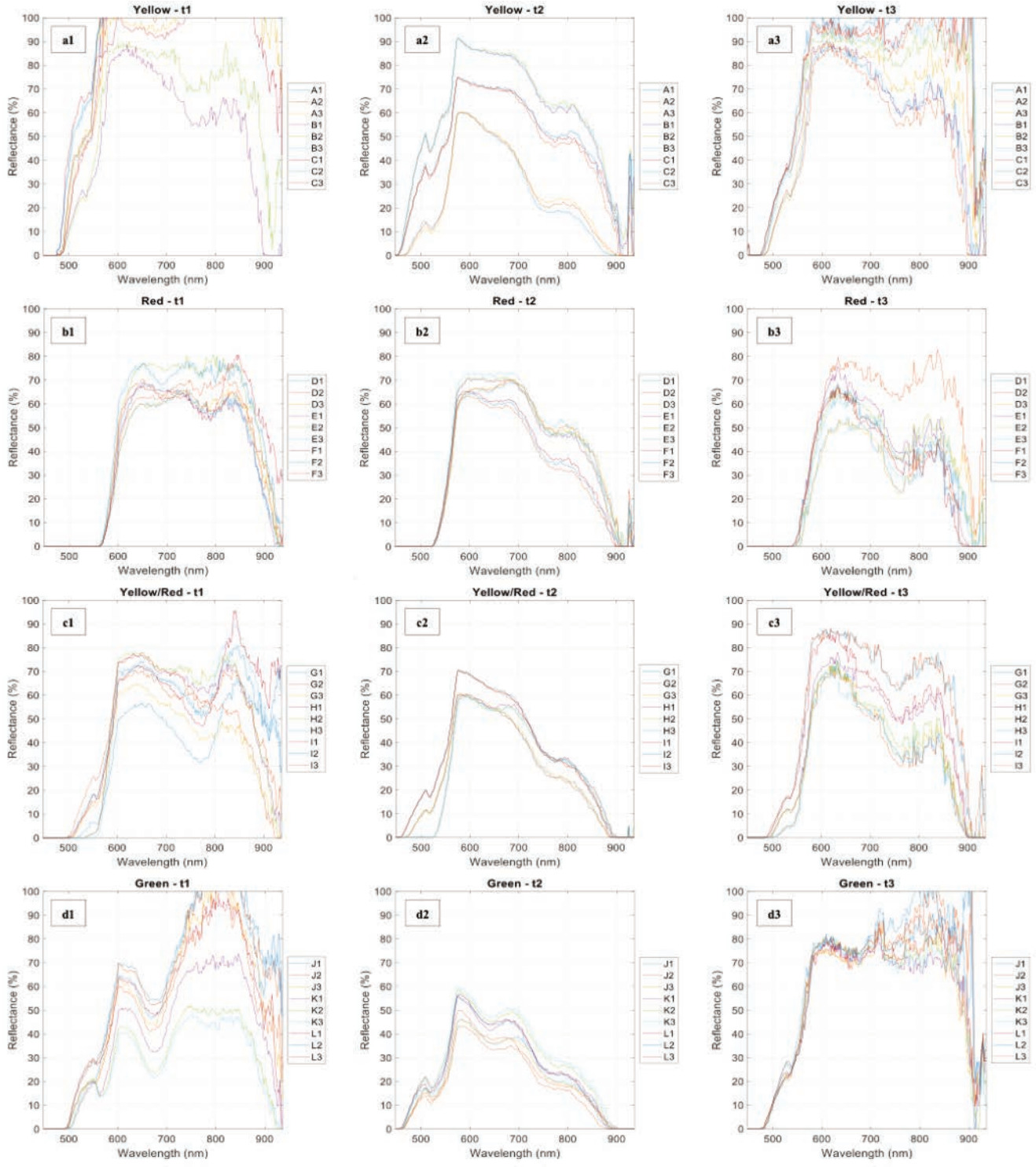


Figure 15. Normalized and averaged spectra of each replica extracted from the left first order of diffraction obtained with the polyester grating at each time point (*i.e.*, t1, t2, and t3): (**a**) yellow apples; (**b**) red apples; (**c**) yellow-red apples; (**d**) green apples.

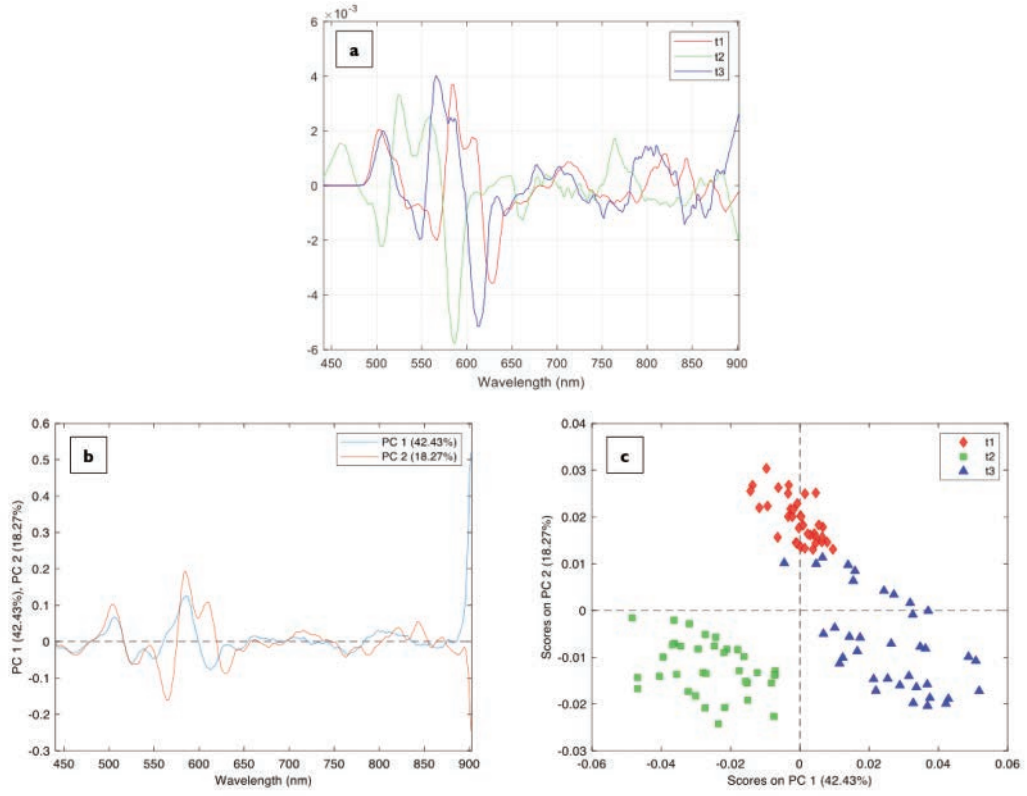


Figure 16. PCA performed on the spectra obtained with the glass-based grating: (**a**) averaged data for each time and pre-processed with SNV and SG second derivative; (**b**) loadings plot; (**c**) scores plot of PC1 and PC2.

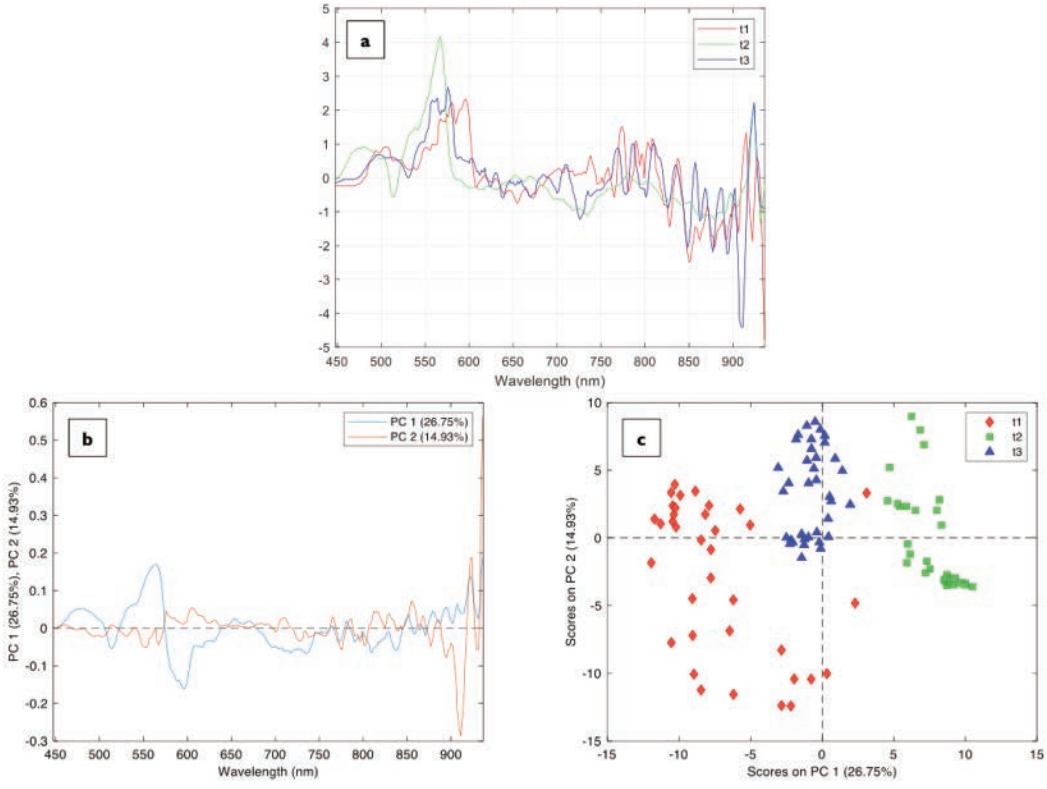


Figure 17. PCA performed on the spectra obtained with the polyester grating: (**a**) averaged data for each time and pre-processed with SNV and SG second derivative; (**b**) loadings plot; (**c**) scores plot of PC1 and PC2.

Good results were also obtained from PCA performed on the spectra from the polyester grating. From the loadings plot (Figure 20b) a sort of equilibrium between the visible and the NIR spectral range was evident in both the principal components. A distinction between healthy and damaged tissues was observed along PC1 (Figure 20c), whereas PC2 exhibited greater capability in differentiating between the two phases of tissue ageing in the damaged tissue (Figure 20d).

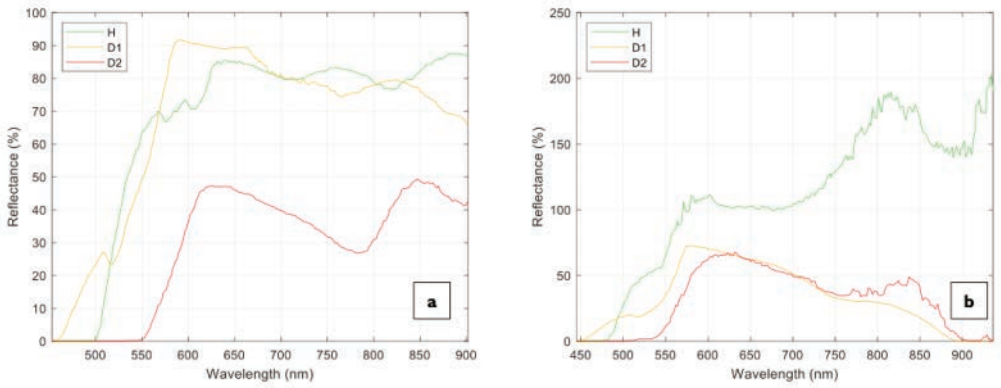


Figure 18. Normalized and averaged spectra obtained with (**a**) glass-based grating and (**b**) polyester grating of yellow apples with healthy tissues (H), and with damaged tissues at two subsequent time points (D1 and D2).

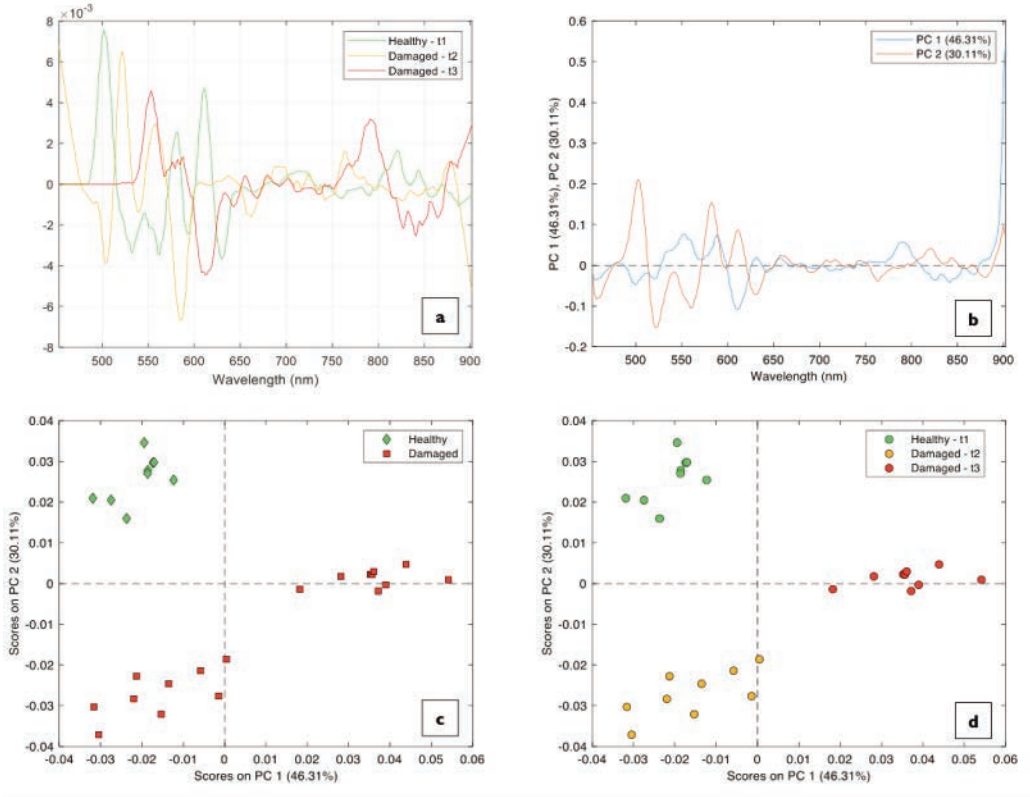


Figure 19. PCA performed on the spectra obtained with the glass-based grating: (**a**) averaged data for each time and pre-processed with SNV and SG second derivative; (**b**) loadings plot; (**c**) scores plot with samples coloured by the tissue type; (**d**) scores plot with the samples coloured by the type of tissues and time of damage.